

# $\text{Au}_x\text{Ag}_y@Zr\text{O}_2$ core–shell nanoparticles: synthesis, characterization, reactivity and optical limiting

A. Sreekumaran Nair<sup>a</sup>, V. Suryanarayanan<sup>a</sup>, T. Pradeep<sup>a,\*</sup>, Jinto Thomas<sup>b</sup>,  
M. Anija<sup>b</sup>, Reji Philip<sup>b</sup>

<sup>a</sup> Department of Chemistry and Sophisticated Analytical Instrumentation Facility, Indian Institute of Technology Madras,  
Chennai 600036, India

<sup>b</sup> Optics Group, Raman Research Institute, Bangalore 560080, India

Received 29 June 2004; received in revised form 31 October 2004; accepted 18 November 2004

## Abstract

$\text{Au}_x\text{Ag}_y@Zr\text{O}_2$  redispersible core–shell nanoparticles were prepared by a single step synthesis using the dimethyl formamide (DMF) reduction procedure. The material is stable for extended periods of time. The core–shell alloy nanoparticles were characterized by UV–vis spectroscopy, transmission electron microscopy, X-ray diffraction, differential scanning calorimetry and cyclic voltammetry. The as prepared particles are nanocrystalline in nature, but they give well-defined diffraction patterns upon heating to 100 °C for 8 h. The average diameter of the core is ~35 nm and typical shell thickness is 2–3 nm. The materials show interesting reactivity with halocarbons as in the case of naked metal nanoparticles, which vary with the composition of the alloy. Our experiments show that oxide-protected alloy nanoparticles are excellent optical limiters in the nanosecond regime. Optical nonlinearity of these systems has been investigated in detail and a qualitative model has been proposed. To the best of our knowledge, this is the first report of nanoparticles having a true alloy core and an oxide shell.

© 2004 Elsevier B.V. All rights reserved.

**Keywords:** Core–shell nanoparticles; Plasmon excitation; Halocarbon reactivity; Optical limiting

## 1. Introduction

Physical and chemical properties of small particles in the nanometer regime differ significantly from those of bulk and as a result, research on nanoparticles has taken many directions in recent years [1–3]. Combinations of Ag and Au have been extensively studied because of the great interest in their plasmon band [4]. Bimetallic colloids are interesting from a number of perspectives, such as their unique electronic, catalytic and optical properties [5–7]. The two main groups of bimetallic colloids are the alloys and layered (core–shell) materials [8–16]. Bimetallic colloids can be prepared by the

simultaneous reduction of two kinds of metal ions with or without the protecting agent or by the successive reduction of one metal over the nuclei of the other [17]. They are excellent substrates for surface enhanced Raman spectroscopy (SERS) [18–19]. A brief history on the synthesis and characterization of alloy nanoparticles can be summarized as follows. Esumi and co-workers prepared Au–Ag colloids in laponite suspensions [6]; Au–Ag colloids immobilized in imogolite fibres were prepared by Liz-Marzan and Philipse [20]. Hostetler et al. synthesized thiolate protected Ag–Au alloy clusters [21]. Shi et al. prepared Ag–Au alloys by putting Ag and Au particles in mesoporous silica by annealing method [22]. Sandhyarani and Pradeep reported a study on thiolate protected crystalline solids of Au–Ag alloys [15]. The simultaneous reduction of  $\text{AgNO}_3$  and  $\text{HAuCl}_4$  with sodium citrate was used by Link et al. for the synthesis of Au–Ag alloys [11]. Papavassiliou prepared alloy nanoparticles of Au and Ag in

\* Corresponding author. Tel.: +91 44 2257 0509;  
fax: +91 44 2257 0509/0545.

E-mail addresses: pradeep@iitm.ac.in (T. Pradeep), reji@rri.res.in (R. Philip).

2-butanol by evaporation and condensation of bulk alloys [23]. Freeman et al. prepared bimetallic colloids with Au core and Ag shell by consecutive reduction of  $\text{HAuCl}_4$  and  $\text{AgNO}_3$  by sodium citrate [19]. Colloids of similar composition were prepared by Morriss and Collins by a slightly different procedure involving the reduction of  $\text{HAuCl}_4$  solution by pure phosphorous and successive reduction of  $\text{Ag}_2\text{O}$  by  $\text{NH}_2\text{OH}\cdot\text{HCl}$  [24]. Mulvaney et al. reported the deposition of gold onto radiolytically prepared Ag sol by re-irradiation of  $\text{KAu}(\text{CN})_2$  solution and Treguer et al. reported the synthesis of layered colloids by radiolysis of a mixed  $\text{Au}^{\text{III}}/\text{Ag}^{\text{I}}$  solution [16]. Recently, the solution phase synthesis of sub-10 nm (Au–Ag) alloy nanoparticles has been reported by Mallin and Murphy [8].

In this paper we report a single step synthesis and characterization of  $\text{Au}_x\text{Ag}_y@\text{ZrO}_2$  core–shell alloy nanoparticles of varying composition. We were prompted to look at this possibility because of our earlier successful work on coating Au and Ag nanoparticles with  $\text{ZrO}_2$  [25]. Research work involving alloy nanoparticles with an oxide cover is limited and we believe that this is the first report on coating of true alloy nanoparticles with an oxide by a single step procedure using solution chemistry. Ag and Au were chosen because of their similarity in atomic sizes and complete miscibility of this pair of metals is obtained in the bulk with little or no change in lattice parameters [26].

## 2. Experimental

$\text{HAuCl}_4\cdot 3\text{H}_2\text{O}$  and  $\text{AgNO}_3$  were purchased from CDH chemicals. Zirconium(IV) propoxide was from Aldrich. All the solvents used in the synthesis were from local sources and were distilled prior to use. The chemicals were of the best purity available. The purity was not independently checked except for UV–vis absorption spectroscopy, wherever necessary. The synthesis of  $\text{Au}_x\text{Ag}_y@\text{ZrO}_2$  core–shell alloy nanoparticles was done by the DMF reduction procedure used for the synthesis of  $\text{Au}@\text{ZrO}_2$  and  $\text{Ag}@\text{ZrO}_2$ . According to the procedure, a solution containing equimolar (20 mM) amounts of zirconium (IV) propoxide and acetyl acetone in 40 ml 2-propanol was prepared. Another solution containing a predetermined number of moles of gold and Ag ions (in the form of  $\text{HAuCl}_4\cdot 3\text{H}_2\text{O}$  and  $\text{AgNO}_3$ ) in a solution of DMF and water (15 and 5 ml, respectively) was prepared. The solutions were mixed and stirred for about 5 min. To avoid the precipitation of  $\text{AgCl}$  (in case excess  $\text{HCl}$  was present in  $\text{HAuCl}_4\cdot 3\text{H}_2\text{O}$ ), the sample was vacuum dried or recrystallized to remove  $\text{HCl}$ . The mixture was transferred to a heating mantle and refluxed for 45 min. The core–shell alloy nanoparticles having compositions  $\text{Au}_{0.18}\text{Ag}_{0.82}@\text{ZrO}_2$ ,  $\text{Au}_{0.3}\text{Ag}_{0.7}@\text{ZrO}_2$  and  $\text{Au}_{0.46}\text{Ag}_{0.54}@\text{ZrO}_2$  were prepared this way. The colors of the solutions vary depending on the composition of the alloys and the thickness of the oxide shell [27]. The  $\text{Au}_{0.18}\text{Ag}_{0.82}@\text{ZrO}_2$  colloid is bluish whereas  $\text{Au}_{0.46}\text{Ag}_{0.54}@\text{ZrO}_2$  is wine red. The  $\text{Au}_{0.3}\text{Ag}_{0.7}@\text{ZrO}_2$  al-

loy has a color intermediate between the other two. The colloidal material was precipitated by the addition of toluene. No metal ions were detected in the supernatant. The precipitate was washed repeatedly with toluene and it was re-dispersed in 2-propanol. The solutions (mother liquor as well as re-dispersed) were stable for extended periods. The UV–vis spectra were recorded with a Perkin-Elmer Lambda 25 spectrometer. Bright-field transmission electron microscope images were taken using a JEOL 3010 high-resolution transmission electron microscope (HRTEM) operated at 300 keV. Samples for transmission electron microscopy were prepared by dropping a dispersion of the particles on copper grid supported Formvar films. X-ray diffraction measurements were taken with Shimadzu XD-D1 diffractometer with  $\text{Cu K}\alpha$  radiation (30 kV, 20 mA). The samples were spread on antireflection glass slides and were wetted with acetone to obtain a uniform film. Acetone was blown dry and the slide was mounted on the diffractometer. Infrared spectra were measured using Perkin-Elmer Spectrum One spectrometer. The samples were made in the form of 1% (by weight) KBr pellets. Differential scanning calorimetric data were acquired with a Netzsch PHOENIX DSC 204 instrument. A total of 10 mg of the samples encapsulated in aluminium pans were used. The measurements were conducted in the temperature range of 20–200 °C. A scan speed of 10 °C  $\text{min}^{-1}$  was used in the measurements. Cyclic voltammograms were obtained with an Electrochemical Analyzer (CH Instruments model 600A) in a standard three-electrode cell comprising of Pt disk (area = 0.8  $\text{mm}^2$ ) as working electrode, platinum foil as counter electrode and  $\text{Ag}/\text{AgCl}$  as the reference electrode. The solvent-supporting electrolyte was acetonitrile containing 0.1 M tetrabutylammonium hexafluorophosphate ( $\text{TBAF}_6\text{P}$ ). Optical limiting measurements were carried out in solution, using 7 ns, 532 nm laser pulses obtained from a frequency-doubled Nd:YAG laser (Spectra Physics, GCR-150). Solutions were prepared by dissolving the samples in 2-propanol, and were taken in a 1 mm cuvette. The laser pulses were plane polarized with a Gaussian spatial profile. The intensity dependent light transmission through the sample was measured using an automated  $z$ -scan [28] set-up. In the  $z$ -scan technique, the laser beam is focused using a lens, and the sample is moved along the beam axis ( $z$ -axis) from one side of the focus to the other, through the focal point. At each position  $z$ , the sample sees different laser fluence, and it will be maximum at the focal point (where  $z$  is taken as zero). An energy meter placed after the sample measures the position dependent (i.e. fluence-dependent) transmission through the sample. In our experiment we added another detector, which is a photo multiplier tube (PMT), to record scattered radiation from the sample [29]. The PMT is kept at a radial distance of 5 cm from the beam axis. Both the PMT and the cuvette are mounted on the same translation stage, so that they remain at the same relative distance throughout the scan. Using an adaptive algorithm, readings were taken at  $z$  intervals of 25  $\mu\text{m}$  around the focal region, which evenly increased to 250  $\mu\text{m}$  for large values of  $z$ .

### 3. Results and discussion

Fig. 1 shows the absorption spectra of core-shell alloy nanoparticles as a function of varying Au content. Traces a, b and c represent the UV-vis spectra of the three alloys having compositions  $\text{Au}_{0.18}\text{Ag}_{0.82}@ZrO_2$ ,  $\text{Au}_{0.3}\text{Ag}_{0.7}@ZrO_2$  and  $\text{Au}_{0.46}\text{Ag}_{0.54}@ZrO_2$ .  $\text{Au}_{0.18}\text{Ag}_{0.82}@ZrO_2$  (trace a) has the absorption maximum at 479 nm. The absorption maxima of  $\text{Au}_{0.3}\text{Ag}_{0.7}@ZrO_2$  and  $\text{Au}_{0.46}\text{Ag}_{0.54}@ZrO_2$  are 511 and 528 nm, respectively. With increase in the mole fraction of gold (from a to c), the peak maximum red shifts, as expected [11]. Note that the peak-width increases with increase in the amount of silver, which implies an increase in the particle size with increase in Ag content as was shown in the case of naked alloy nanoparticles [20]. For bare alloy nanoparticles of Au and Ag of composition  $\text{Au}_{0.27}\text{Ag}_{0.73}$ ,  $\text{Au}_{0.54}\text{Ag}_{0.46}$ , and  $\text{Au}_{0.8}\text{Ag}_{0.2}$ , the plasmon absorption maxima occur at 430, 455 and 480 nm, respectively [11]. These particles are citrate protected and have an average size 20 nm. The larger shift observed in the present case from the above linear composition dependence of peak maximum is attributed to the combined effect of the increased particle size and the presence of the dielectric shell around the alloy core. The nature of the absorption spectra is explainable in terms of Mie's theory [30]. UV-vis spectroscopy can be easily applied to differentiate an alloy structure from that of a core-shell one (Ag@Au or Au@Ag) for Au-Ag bimetallic particles. Two plasmon absorption peaks may be expected for Ag@Au, Au@Ag and a solution containing a mixture of nano Au and Ag colloids [9,31]. Analysis of the absorption spectra based on Mie's theory supports our claim that the nanoparticles are true alloys and not Au@Ag or Ag@Au [32]. Blue shift in the plasmon band accompanied by broadening with increase in mole fraction of silver further supports the alloy structure. Even though the exact mechanism of alloy formation is not clear,

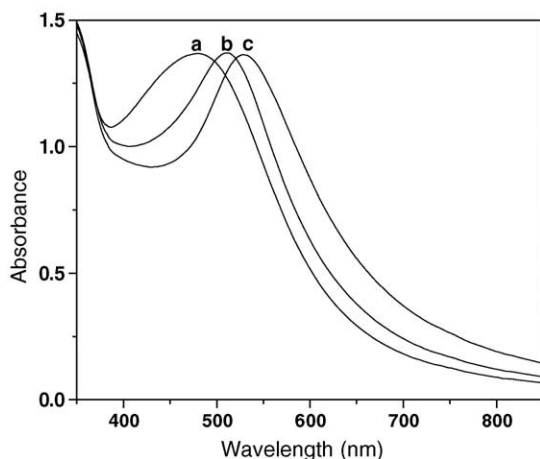


Fig. 1. The UV-vis spectra of three alloys having compositions: (a)  $\text{Au}_{0.18}\text{Ag}_{0.82}@ZrO_2$ ; (b)  $\text{Au}_{0.3}\text{Ag}_{0.7}@ZrO_2$ ; and (c)  $\text{Au}_{0.46}\text{Ag}_{0.54}@ZrO_2$ . Note that the spectra red shift with increase in the mole fraction of gold. There is also a slight increase in the bandwidth with increase in silver mole fraction because of the increase in particle size.

it is suggested that alloying occurs due to fast inter-diffusion of atoms at the surface. As the melting point of smaller particles (although smaller than the size regime investigated here) is much lower than that of bulk, the diffusion coefficient in nanoparticles is expected to be many orders of magnitude larger than in bulk [32,33]. It is also believed that interfacial imperfections enhance diffusion of atoms by several orders of magnitude [34], thereby enhancing the alloying process.

A bright field TEM image of the alloy having composition  $\text{Au}_{0.46}\text{Ag}_{0.54}@ZrO_2$  is shown in Fig. 2. As shown by UV-vis spectroscopy, TEM image confirms the formation of true alloys, rather than Au@Ag or Ag@Au. Various morphologies of the core-shell particles are visible, including those with circular, hexagonal and triangular projections; circular and thus spherical particles being the most common. The  $ZrO_2$  shell around the alloy nanoparticles is visible in the slightly overfocussed condition. It may be noted that the contrast of the shell against the strongly scattering alloy core is fairly weak and as a result of this, the shell structure is not well defined. A large size distribution of particles is visible in the TEM images; the average particle size is 35 nm, and the typical shell thickness is 2–3 nm, which were confirmed by X-ray diffraction studies also (see below). The inset shows an isolated core-shell nanoparticle. The contrast difference within the metallic core suggests its true alloy nature [10]. Improved images with a clear, lattice resolved shell structure is obtainable by monolayer functionalization of the shell, as we have shown in the case of Ag@ $ZrO_2$  [35]. No isolated  $ZrO_2$  or metallic particles were seen in the images.

Fig. 3A shows another large area image of the same sample showing the core-shell geometry of the particles. Fig. 3B

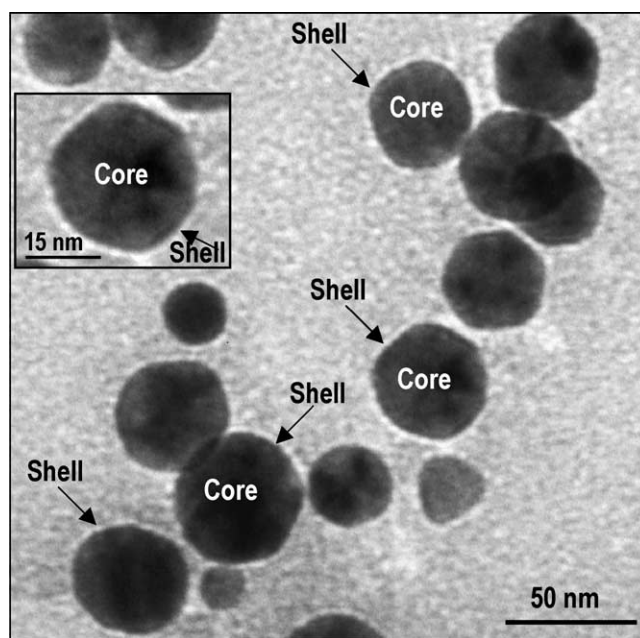


Fig. 2. A transmission electron micrograph of the  $\text{Au}_{0.46}\text{Ag}_{0.54}@ZrO_2$  core-shell nanoparticles. The core and the shell are clearly visible. The average core dimension is  $\sim 35$  nm and the typical shell thickness is 2–3 nm.

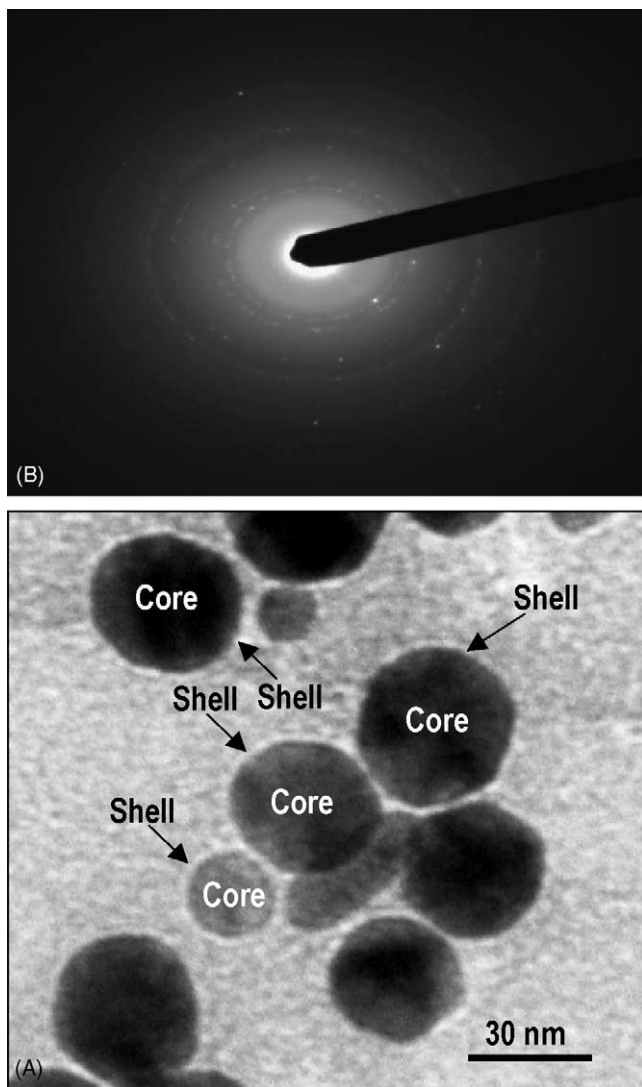


Fig. 3. (A) A large area transmission electron micrograph of the alloy nanoparticles showing the core and shell regions. (B) The electron diffraction pattern of the same material from the fcc lattice. The diffused diffraction pattern shows the nanocrystalline nature of the as prepared material.

shows the electron diffractogram of the same sample. The diffractogram is not well defined due to the nano-crystalline nature of the as prepared material.

Two X-ray diffractograms (XRD) of the alloy nanoparticles are shown in Fig. 4. Fig. 4A and B represents the diffractograms of the air-dried (at room temperature) alloy having a composition of  $\text{Au}_{0.3}\text{Ag}_{0.7}/\text{ZrO}_2$  and the same after drying at  $100^\circ\text{C}$  for 8 h, respectively. The material dried at room temperature (air-dried) gives no strong diffraction peaks, except perhaps a peak in the correct position for the (1 1 1) reflection of the fcc metal core. We can therefore conclude that at room temperature the material is either mostly amorphous or the crystallites are extremely small. The latter would concur better with the TEM observations. But materials dried at  $100^\circ\text{C}$  for 8 h show diffraction patterns of monoclinic  $\text{ZrO}_2$  and the alloy core (marked in Fig. 4B). The average size of the core

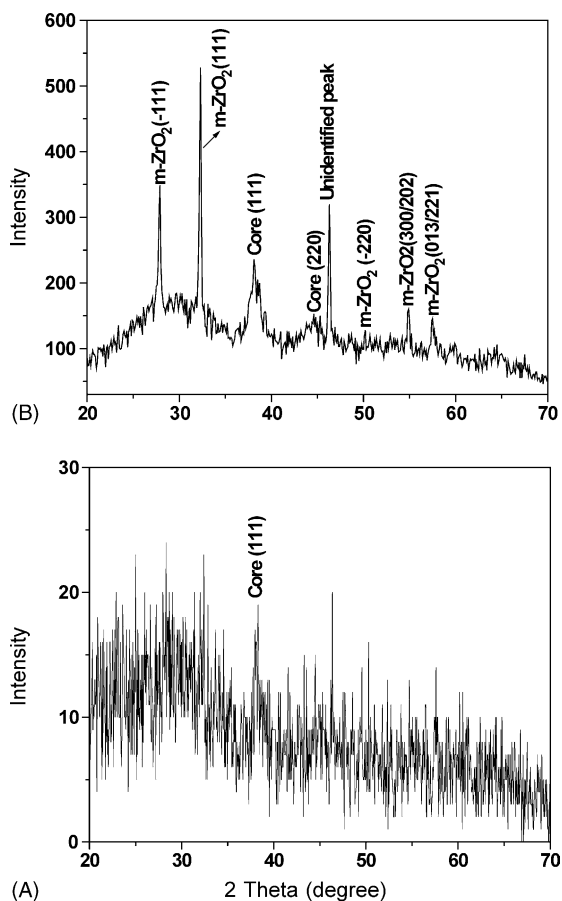


Fig. 4. The X-ray diffraction pattern of the alloy having composition  $\text{Au}_{0.3}\text{Ag}_{0.7}/\text{ZrO}_2$ . The diffractogram (A) is that of the air-dried sample and (B) is that of the same material dried at  $100^\circ\text{C}$  for 8 h. The powders dried at  $100^\circ\text{C}$  for 8 h show well-defined diffraction patterns. The diffraction patterns from monoclinic  $\text{ZrO}_2$  shell and (Au–Ag) alloy core (marked in (B)) are seen in the diffractograms.

from the XRD measurements after  $100^\circ\text{C}$  heat treatment is 33 nm and that of the  $\text{ZrO}_2$  shell is  $\sim 3.2$  nm. It may be noted that the normal room temperature monoclinic structure of zirconia was retained after heating to  $250^\circ\text{C}$  for 8 h. Diffraction measurements on all the other compositions gave similar information. XRD of the sample dried at  $250^\circ\text{C}$  gave a narrower peak for the core (suggesting crystal growth), but the zirconia peaks did not manifest any significant change. The crystallization of  $\text{ZrO}_2$  shell on heating was also confirmed by infrared spectroscopic measurements (Fig. 5). Trace a is the infrared spectrum of the air-dried sample and b, c and d are that of the same sample heated at 100, 200 and  $300^\circ\text{C}$ , respectively. The emergence of monoclinic  $\text{ZrO}_2$  features at  $643$  (asymmetric Zr–O–Zr stretching mode, arising from the fully symmetric coupling of the  $B_1$  and  $B_2$  modes) and at  $614\text{ cm}^{-1}$  (fully symmetric coupling of the  $A_1$  modes of monoclinic  $\text{ZrO}_2$ ) on heating is evident from the IR traces [36].

Differential scanning calorimetric traces (Fig. 6) of the nanocrystalline alloys show an irreversible transition attributed to the crystallization of the shell, which is dependent on the composition of the alloy. We believe that the shell crys-

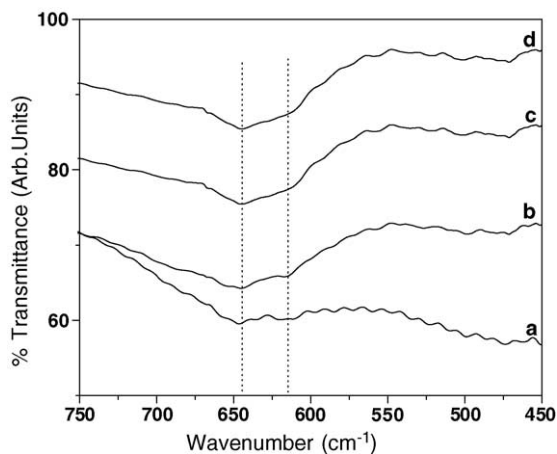


Fig. 5. Temperature dependent IR spectra of the alloy having a composition of  $(\text{Au}_{0.3}\text{Ag}_{0.7})@\text{ZrO}_2$ . Trace a is the IR spectrum of the sample at room temperature. Traces b, c and d are the IR traces of the same sample dried at 100, 200 and 300 °C, respectively. As can be seen, the IR features of monoclinic  $\text{ZrO}_2$  have emerged as a result of heating. The peak at  $643\text{ cm}^{-1}$  corresponds to the asymmetric Zr–O–Zr stretching mode arising from the fully symmetric coupling of the  $B_1$  and  $B_2$  modes and the shoulder ( $A_1g$ ) seen at  $614\text{ cm}^{-1}$  may be due to the fully symmetric coupling of the  $A_1$  modes of monoclinic  $\text{ZrO}_2$ .

tallization along with crystal growth and elimination of grain boundaries, twins, etc. resulted in the broad endotherm, rather than a sharp feature. The transition temperature is centered in the 105–120 °C range for all the three alloys. The alloy with composition  $\text{Au}_{0.46}\text{Ag}_{0.54}@\text{ZrO}_2$  shows the transition temperature of 106.4 °C (trace a). The other two alloys with compositions,  $\text{Au}_{0.3}\text{Ag}_{0.7}@\text{ZrO}_2$  and  $\text{Au}_{0.18}\text{Ag}_{0.82}@\text{ZrO}_2$  show peak maxima of 108 and 112.4 °C, respectively (traces b and c). The DSC data suggest that the transition temperature is dependent on its composition and that increase in gold content in the alloy brings about a decrease in the transition temper-

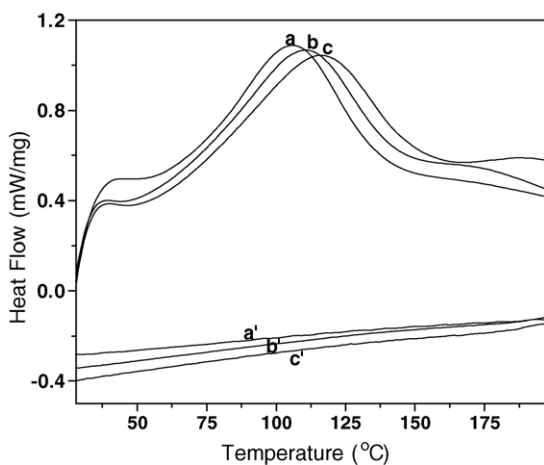


Fig. 6. The DSC traces of the three alloys having compositions: (a)  $\text{Au}_{0.46}\text{Ag}_{0.54}@\text{ZrO}_2$ ; (b)  $\text{Au}_{0.3}\text{Ag}_{0.7}@\text{ZrO}_2$ ; and (c)  $\text{Au}_{0.18}\text{Ag}_{0.82}@\text{ZrO}_2$ . The transition temperature corresponding to the crystallization of shell is composition dependent. Note the decrease in transition temperature with increase of gold mole fraction. The peak below 50 °C in all the samples in the forward scan is attributed to solvent desorption.

ature. The core–shell materials,  $\text{Au}@\text{ZrO}_2$  and  $\text{Ag}@\text{ZrO}_2$  also show this behavior in DSC and their transition temperatures are 95 and 126 °C, respectively. It must be noted that the transition temperatures of all the three alloys are intermediate of these two values. As the cores in the pure metal systems ( $\text{Au}@\text{ZrO}_2$  and  $\text{Ag}@\text{ZrO}_2$ ) are crystalline, the transition observed in the DSC cannot be due to melting of the core. This is the reason we attribute the heat change to shell crystallization and crystal growth by removal of grain boundaries, twins, defects, etc. It may be noted that the crystallization occurs at a reduced temperature as the particle size decreases. It also appears that the shell crystallization induces annealing of the core. Thus the enthalpy corresponding to the transition is a composite of both the events. Enthalpy decreases marginally with increase in Ag composition; this could be because of the slight decrease in the fractional amount of  $\text{ZrO}_2$  as the particle size increases; there can be other factors as well. The decrease in transition temperature for gold-rich alloys could be because of their smaller size, consequently the reduced shell dimension.

Cyclic voltammograms (CVs) were recorded in order to characterize these nanocomposite alloy materials based on their redox chemistry in the solution phase. It must be noted that electron transport is possible through the shell [25,37–39]. Typical CV of Ag and Au alloy nanomaterials with different compositions, represented as (a)  $\text{Au}_{0.46}\text{Ag}_{0.54}@\text{ZrO}_2$ ; (b)  $\text{Au}_{0.3}\text{Ag}_{0.7}@\text{ZrO}_2$ ; and (c)  $\text{Au}_{0.18}\text{Ag}_{0.82}@\text{ZrO}_2$ , taken in the  $\text{CH}_3\text{CN}/\text{TBAHFP}$  solvent-supporting electrolyte system at a sweep rate of  $0.3\text{ V s}^{-1}$  are shown in Fig. 7. For comparison, cyclic voltammograms of  $\text{Au}@\text{ZrO}_2$  and  $\text{Ag}@\text{ZrO}_2$  recorded at the same sweep rate are also shown in Fig. 7 as insets A and B, respectively [25]. During the scanning,  $\text{Au}@\text{ZrO}_2$  shows a characteristic reversible redox couple centered at  $E_{1/2} = 0.330$  and 0.280 V, respectively, with a peak separation,  $\Delta E_p$  of 0.066 V versus  $\text{Ag}/\text{AgCl}$  [25] (Fig. 7, inset A). The anodic and cathodic

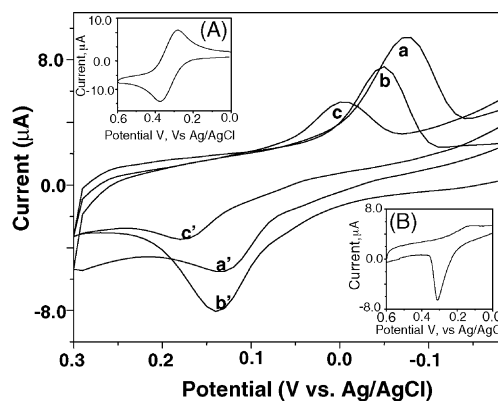


Fig. 7. Cyclic voltammograms of (a)  $\text{Au}_{0.46}\text{Ag}_{0.54}@\text{ZrO}_2$ ; (b)  $\text{Au}_{0.3}\text{Ag}_{0.7}@\text{ZrO}_2$ ; and (c)  $\text{Au}_{0.18}\text{Ag}_{0.82}@\text{ZrO}_2$  alloy nanoparticles recorded on Pt electrode in  $\text{CH}_3\text{CN}$  containing 0.1 M tetrabutylammonium hexafluorophosphate at a sweep rate of  $0.3\text{ V s}^{-1}$ . The insets (A) and (B) show CVs of  $\text{Au}@\text{ZrO}_2$  and  $\text{Ag}@\text{ZrO}_2$ , respectively, which were taken under identical experimental conditions at the same sweep rate.

current ratio of unity also confirms the perfectly reversible nature of the system. The sharp and symmetrical anodic peak at this potential suggests one-electron transfer reaction characteristic of the gold nanoparticles [40] ( $Au_n \rightarrow Au_n^+ + e$ ). The voltammetry was significantly different for the alloy materials. Typical CV of the zirconium oxide coated alloy material  $Au_{0.46}Ag_{0.54}$  recorded under the same experimental conditions is shown in Fig. 7a. With the incorporation of Ag to Au, both the anodic and cathodic peak potentials abruptly shift to 0.145 and  $-0.080$  V. The redox property of  $Au_n/Au_n^+$  is changed from reversible to quasi-reversible nature with a peak separation,  $\Delta E_p$  of 0.200 V. When the silver content was further increased; as in the case of alloys such as  $Au_{0.3}Ag_{0.7}@ZrO_2$  and  $Au_{0.18}Ag_{0.82}@ZrO_2$ , the voltammograms shift considerably towards the anodic side (curves b and c). The cathodic current also decreases two-fold from b to c (Fig. 7). This shift in potential towards the anodic side with increasing silver content makes the alloys more stable in their electrochemical oxidation or reduction (in this medium) behavior. Quasi-reversibility is found in these two cases as well with the same  $\Delta E_p$ . Note that pure  $Ag@ZrO_2$  maintains the characteristic quasi-reversible redox nature, centered at  $E_{1/2} = 0.215$  V with further shift of anodic peak and cathodic peak in the same direction along with a  $\Delta E_p$  of 190 mV (Fig. 7, inset B) [37]. The surface coverage calculated from the area under the anodic peak is found to be larger than the cathodic peak. This redox couple is assigned to the electrochemical oxidation,  $Ag_n \rightarrow Ag_n^+ + e$ . With the increasing sweep rate, both the anodic and cathodic peak currents of the alloy materials increase; a graph of peak current versus square root of sweep rate is linear which also passes through the origin. This shows that the electrochemical process is diffusion controlled in the solution phase. The characteristic peak potential also shifts linearly with increasing sweep rate. Thus the electrochemical response of the alloys is also composition dependent.

The halocarbon reactivity [41] of metal nanoparticles has been studied with benzyl chloride. The reaction of  $Au@ZrO_2$  and  $Ag@ZrO_2$  with halocarbons leads to the selective leaching of metal core resulting in the formation of metal oxide nanobubbles [39]. This experiment was done to check whether the shells behave similar to those on pure metal cores in terms of molecular diffusion. To 3.5 ml of the as prepared alloy nanoparticle solution, 100  $\mu$ l of benzyl chloride was added and the progress of the reaction was monitored in a time dependent manner by UV-vis spectroscopy. Fig. 8A shows the reaction of the alloy having composition  $Au_{0.3}Ag_{0.7}@ZrO_2$  with benzyl chloride. Trace a is the absorption spectrum of the pure alloy having the absorption maximum of 511 nm. Trace b was recorded just after the addition of 100  $\mu$ l of benzyl chloride. The reduction in the plasmon absorption as well as its red shift is due to the reaction between the alloy core and the halocarbon. Subsequent traces (up to r) were recorded at an interval of 20 min. The plasmon absorption maximum shifts from 511 to 531 nm as a result of the reaction with benzyl chloride. The red shift could

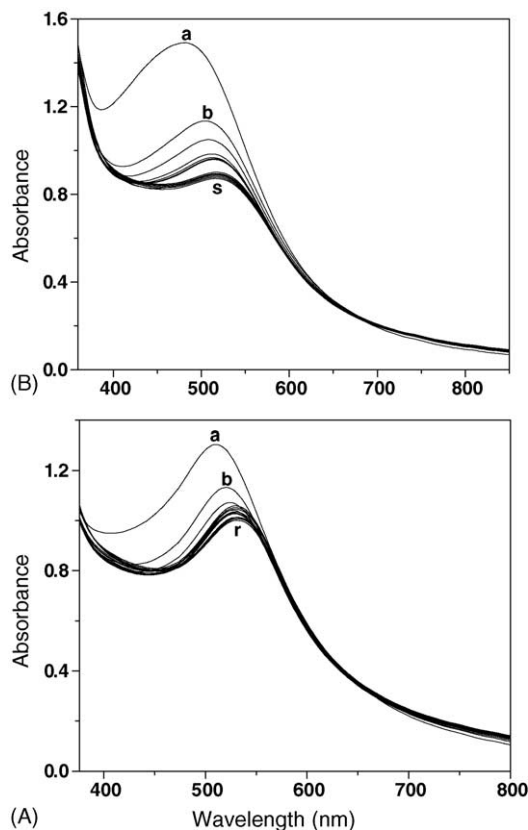


Fig. 8. Time dependent UV-vis spectra showing the effect of adding benzyl chloride to the two types of alloys having compositions: (A)  $Au_{0.3}Ag_{0.7}@ZrO_2$  and (B)  $Au_{0.18}Ag_{0.84}@ZrO_2$ . Trace a is the absorption spectrum of the pure cluster. Trace b was taken immediately after the addition of benzyl chloride. Subsequent traces (up to “r” in (A) “s” in (B)) were taken at 20 min interval. The reactivity as well as red shift is more pronounced in the case of alloy having high mole fraction of silver (B). In both cases, as the reaction progresses, there is a reduction in absorbance as well as a red shift of peak maximum because of selective removal of silver from the alloy. A small increase in background is visible for the traces (b–r) in A and (b–s) in (B) because of the formation of  $AgCl$ , which makes the solution partly cloudy and hence some scattering in the absorption spectra. After the complete removal of silver, no further red shift is seen even after stirring of the solution for several hours.

be attributed to the selective leaching of Ag from the alloy; making the alloy richer in gold. The red shift continues till all the silver gets removed as  $AgCl$  and thereafter no further red shift is observed even with further stirring of the solution. This may either be due to complete blocking of the pores of  $ZrO_2$  shell by amorphous carbon produced as a result of the reaction [41] or selective removal of Ag leading in asymmetric gold nanostructures, which are stable towards halocarbons. A small increase in the background is visible for the traces (b–s) because of the formation of  $AgCl$ , which makes the solution partly cloudy and hence some scattering in the optical absorption measurements. We have established from reactivity studies on bare metal clusters that Ag is more reactive than Au [41]. Fig. 8B is the time dependent UV-vis spectra showing the reaction of  $Au_{0.18}Ag_{0.82}@ZrO_2$  and benzyl chloride. Note that the reduction in plasmon intensity is abrupt in this

case. The plasmon absorption shifts from 479 to 521 nm as a result of the leaching of Ag from the alloy core. Here also increase in the background due to the formation of AgCl is visible. The composition dependent reactivity of benzylchloride with alloy core-shell nanoparticles is evident from Fig. 8A and B. For the  $\text{Au}_{0.3}\text{Ag}_{0.7}@ZrO_2$  alloy, the absorbance corresponding to the plasmon excitation decreases from 1.30 to 1.13 (a decrease of 0.17) just after the addition of 100  $\mu\text{l}$  of benzylchloride, whereas for the alloy with composition  $\text{Au}_{0.18}\text{Ag}_{0.82}@ZrO_2$ , the decrease in absorbance was 0.36, i.e. from 1.49 to 1.13. Similarly, the red shift in surface plasmon peak was 20 nm in the former, whereas that was 42 nm in the latter. This clearly shows that as the composition of Ag in the alloy core increases, the reactivity towards halocarbons also increases. A very similar trend was observed in the case of the alloy having composition,  $\text{Au}_{0.46}\text{Ag}_{0.54}@ZrO_2$  also. Here the reduction in plasmon peak (0.06 in A) and the red shift (2 nm) just after the addition of benzylchloride were much less than that of the other two cases mentioned above.

Oxide protection renders metal nanoparticles stable under conditions of intense laser irradiation. For example, our recent studies have shown that oxide-protected nanometal particles withstand laser fluences up to  $20\text{ J cm}^{-2}$  without damage [29]. Moreover, protection by shells makes it possible to prepare materials in the form of thin films and disks.

These qualities make them suitable candidates for nonlinear optics and photonics applications. We irradiated the samples with nanosecond laser pulses at 532 nm. Results show that the samples have a nonlinear transmission, which varies as the laser intensity. When the intensity is high, the transmission decreases significantly, showing that they can be used for optical limiting applications.

The  $z$ -scan curves obtained for  $\text{Au}_{0.18}\text{Ag}_{0.82}@ZrO_2$ ,  $\text{Au}_{0.3}\text{Ag}_{0.7}@ZrO_2$  and  $\text{Au}_{0.46}\text{Ag}_{0.54}@ZrO_2$  suspended in 2-propanol are shown in Fig. 9A–C, respectively. For each  $z$  position, the sample transmission obtained is normalized to its linear transmission to get the normalized transmittance which is plotted against  $z$ . Fig. 9D gives the normalized transmittance as a function of the input laser fluence. In general, an increase in transmission is seen at moderate laser fluences, and the net transmission decreases appreciably at higher fluences. However, the detailed features of the nonlinear transmission depend crucially on the alloy composition. As seen from the figure, the transmission increase is highest when the Au mole fraction is largest in the composite. Moreover, the effect is enhanced for higher sample concentrations within each composite. The optical limiting threshold (defined as the fluence at which the normalized transmittance drops to 0.5) is around  $2.4\text{ J cm}^{-2}$ , except for  $\text{Au}_{0.46}\text{Ag}_{0.54}@ZrO_2$ , in which the limiting threshold is much higher.

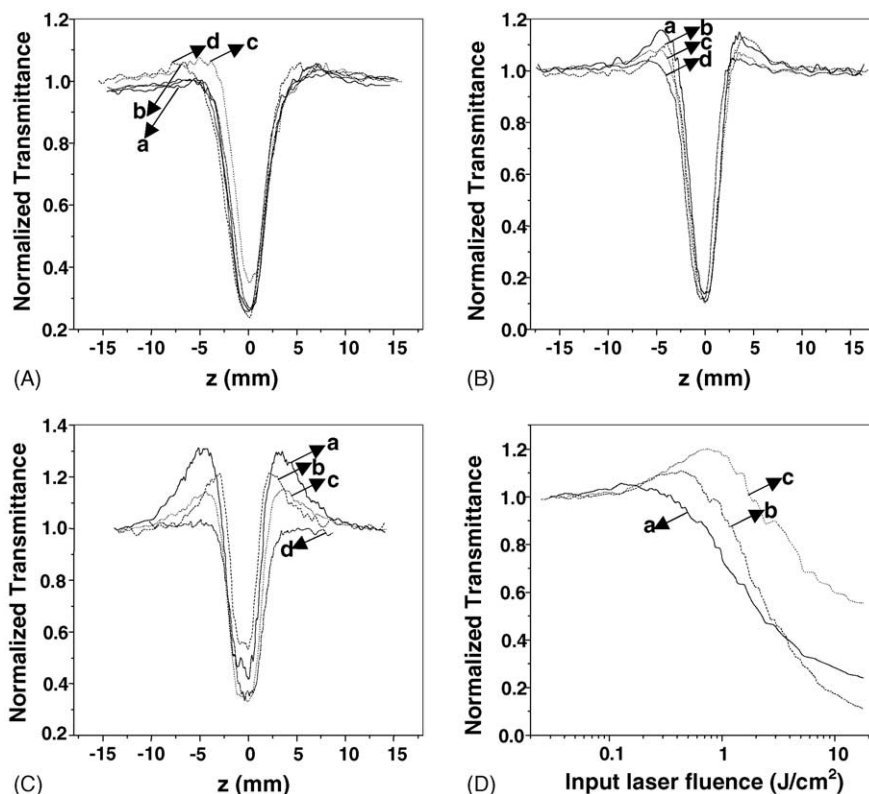


Fig. 9. The  $z$ -scan curves obtained for the samples are shown in (A) ( $\text{Au}_{0.18}\text{Ag}_{0.82}@ZrO_2$ ); (B) ( $\text{Au}_{0.3}\text{Ag}_{0.7}@ZrO_2$ ); and (C) ( $\text{Au}_{0.46}\text{Ag}_{0.54}@ZrO_2$ ). Laser pulse energy used is  $30\text{ }\mu\text{J}$ . Sample linear transmissions at 532 nm are: (a) 40%; (b) 50%; (c) 60%; and (d) 70%. The plasmon band bleach is most prominent in ( $\text{Au}_{0.46}\text{Ag}_{0.54}@ZrO_2$ ). (D) The normalized transmittance as a function of the incident laser fluence, for representative samples having a linear transmission of 50%: (a)  $\text{Au}_{0.18}\text{Ag}_{0.82}@ZrO_2$ ; (b)  $\text{Au}_{0.3}\text{Ag}_{0.7}@ZrO_2$ ; and (c)  $\text{Au}_{0.46}\text{Ag}_{0.54}@ZrO_2$ .

The observed increase in transmission at moderate laser fluences can be explained on the basis of surface plasmons, which exist at the interface between the metal and the surrounding dielectric. Mie's theory [30] attributes the plasmon absorption band of spherical particles to dipolar oscillations of free electrons in the conduction band occupying energy states close to the Fermi energy. The corresponding absorption cross section is given as [4] ( $18\pi V n_0^{3/2}/\lambda$ ) $\epsilon_2/((\epsilon_1 + 2n_0^2)^2 + \epsilon_2^2)$ , where  $V$  is the particle volume,  $n_0$  is the refractive index of the surrounding medium, and  $\epsilon_1$  and  $\epsilon_2$  are the real and imaginary parts of the metal's dielectric response  $\epsilon_m$ . The absorption peak of the surface plasmon resonance (SPR) occurs when  $\epsilon_1 + 2n_0^2 = 0$ , and the SPR bandwidth is related to  $\epsilon_2$ . A singular property of the SPR is that it leads to a large local field enhancement within the metal particle. This effect can be appreciable with laser excitation, where the electric field associated with the electromagnetic radiation is quite high. In the quasi-static limit the local field inside a spherical particle  $E_{loc}$ , is related to the applied field  $E_0$  by  $E_{loc} = [3e_m(w)/e_m(w) + 2e_d(w)]E_0 = f(w)E_0$ , where  $e_d$  is the dielectric constant of the surrounding medium;  $f(w)$  is defined as the local field factor. At the SPR peak the local field factor has the maximum value, given by  $|f_{max}(w_p)|^2 = |3e_1/2e_2|^2$ . Since the real part of the dielectric constant is larger than the imaginary part in noble metals, they experience strong local field enhancements upon laser

irradiation. Therefore, the effective third order nonlinear susceptibility  $c^{(3)}(w)$  will be strongly enhanced in the SPR region [42], and this nonlinearity induces a saturation of absorption, which is generally referred to as "plasmon band bleach" in literature [43,44]. In the present case, we see this bleach in the form of humps flanking the valley in the  $z$ -scan curves. The saturation is most prominent in  $Au_{0.46}Ag_{0.54}@ZrO_2$ , where the Au concentration is the largest. In fact, it is strong enough to push the sample's optical limiting threshold to more than  $20 J cm^{-2}$ , as seen from Fig. 9D. This is a direct consequence of the red shift of the SPR with Au mole fraction, which brings it closer to the excitation wavelength of 532 nm. Therefore, the plasmon band bleach in the alloy system is dependent on its stoichiometry. Fig. 10A shows the relative magnitudes of the bleach, obtained for various sample concentrations.

At higher laser fluences the transmission is found to drop significantly, and this renders practical applicability to the nanoparticles as optical limiters. A reduction in transmission can occur due to a number of phenomena, and the prominence of each will depend on the sample, excitation wavelength and laser pulse width. For example, in organic materials, reverse saturable absorption (RSA) is a major cause of optical limiting while in semiconductors it can be free carrier absorption [45]. However, since we have used nanosecond pulses and the sample consists of spherical particles, we should consider the possibility of nonlinear scattering at high intensities. Scatter-

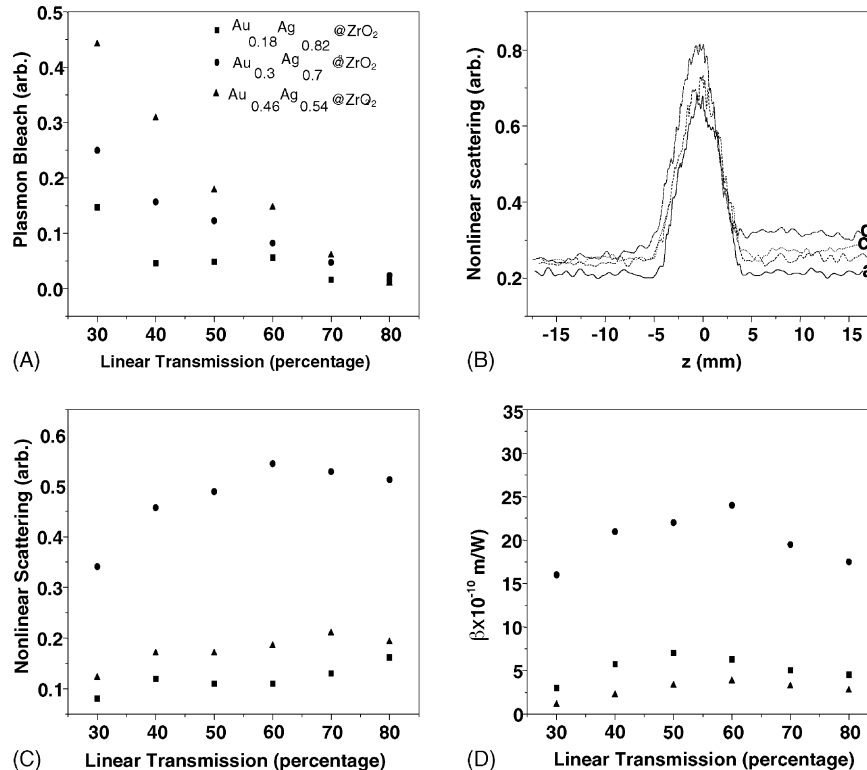


Fig. 10. Variation of the plasmon band bleach with sample concentration is shown in (A). (B) The typical PMT output, obtained for  $Au_{0.3}Ag_{0.7}@ZrO_2$ , showing large nonlinear scattering around the beam focus ( $z=0$ ). Sample linear transmissions are: (a) 40%; (b) 50%; (c) 60%; and (d) 70%. (C) The magnitude of scattering as a function of linear transmission. Numerically calculated values of the nonlinearity coefficient  $\beta$  are given in (D). The symbols correspond to the same composition as in (A).

ing is a fundamental display of light–matter interaction resulting from inhomogeneities in the refractive index, leading to a decrease of net transmission through the medium. Resonant excitation with nanosecond and longer pulses can result in thermally induced transient refractive index changes given by  $\Delta n_0 = (dn_0/dt)F_0\alpha/2\rho C_v$ , where  $dn_0/dt$  is the thermo-optic coefficient,  $F_0$  is the fluence,  $\alpha$  is the density and  $C_v$  is specific heat at constant volume. It has been found that such nonlinear scattering contributes to optical limiting in carbon black [45] and nanotube [46] suspensions, and metal–dendrimer nanocomposites [47]. To find out whether nonlinear scattering is indeed taking place, we monitored the output of the PMT that is located off-axis in our experiment, throughout the  $z$ -scans. The typical result obtained is shown in Fig. 10B. Comparing with Fig. 9, it is seen that the onset of limiting is complementary to the increase in scattering, and the point of maximum limiting coincides with that of maximum scattering. The scattering amplitude as a function of the sample concentration is given in Fig. 10C. A larger scattering is seen at lower concentrations, which probably indicates a better thermal diffusion. Interestingly, the net scattering is highest for  $\text{Au}_{0.3}\text{Ag}_{0.7}@ZrO_2$ , the cause of which is not well understood now. To estimate the absolute strength of this nonlinearity, we numerically evaluated the quantity  $\beta$  by fitting the  $z$ -scan curves to the transmission equation [28]

$$T(z) = \left[ \frac{1}{\pi^{1/2}} q(z) \right] \int_{-\infty}^{+\infty} \ln[1 + q(z) \exp(-\tau^2)] d\tau$$

with  $q(z) = \beta I_0 L / [1 + (z/z_0)^2]$ , where  $I_0$  is the peak intensity at the focal point,  $L = [1 - \exp(-\alpha l)]/\alpha$ , where  $l$  is the sample length and  $\alpha$  is the linear absorption coefficient, and  $z_0 = \pi\omega_0^2/\lambda$  is the Rayleigh range, where  $\omega_0$  is the beam waist radius at focus and  $\lambda$  is the light wavelength;  $\beta$  in the present context represents nonlinear scattering: in general, for different NLO materials, it can signify phenomena like two-photon absorption [28] or reverse saturable absorption as well. As shown in Fig. 10D, the  $\beta$  values have been calculated to be in the order of  $10^{-10} \text{ m W}^{-1}$ . This is a substantial nonlinearity, which is comparable to those found for metal–chalcogenide clusters [49,50] and  $\text{C}_{60}$  solutions [48]. For all the three alloys, the  $\beta$  values are found to peak around a linear transmission of 0.5–0.6.

#### 4. Conclusions

Core–shell alloys having compositions  $\text{Au}_{0.18}\text{Ag}_{0.82}@ZrO_2$ ,  $\text{Au}_{0.3}\text{Ag}_{0.7}@ZrO_2$  and  $\text{Au}_{0.46}\text{Ag}_{0.54}@ZrO_2$  have been synthesized by a one-step route and characterized by various techniques like absorption spectroscopy, transmission electron microscopy, X-ray diffraction, infrared spectroscopy, differential scanning calorimetry and cyclic voltammetry. All studies conclusively established the core–shell nature of the material. The materials are stable for several months and show little aggregation. As prepared materials

appear to be nanocrystalline at room temperature, but upon heating to 100 °C for 8 h show well-defined diffraction peaks corresponding to the core and the shell. Temperature dependent infrared spectroscopy supports the crystallization of the shell at higher temperatures. DSC data support annealing of the shell and the core. Optical measurements reveal that significant nonlinear light scattering occurs in these core–shell alloys at high intensity laser irradiation, making these materials strong optical limiters with a high laser damage threshold. The UV–vis spectra, cyclic voltammetry responses, optical limiting behavior and halocarbon reactivity of the alloys are all composition dependent.

#### Acknowledgements

T.P. acknowledges financial support from the Space Technology Cell of Indian Institute of Technology Madras, and the Ministry of Information Technology for his oxide-protected metal cluster research program. Equipment support was provided by the Nanoscience and Nanotechnology Initiative of the Department of Science and Technology. Dr. Ian MacLaren of Darmstadt University of Technology, Germany is thanked for a critical reading of the manuscript.

#### References

- [1] J.H. Hodak, A. Henglein, G.V. Hartland, *J. Phys. Chem. B* 104 (2000) 204.
- [2] S. Link, M.A. El-Sayed, *J. Phys. Chem. B* 103 (1999) 8410.
- [3] M. Valden, X. Lai, D.W. Goodman, *Science* 281 (1998) 1647.
- [4] U. Kreibitz, M. Vollmer, *Optical Properties of Metal Clusters*, Springer, Berlin, 1995, p. 187.
- [5] Y.H. Chen, U. Nickel, *J. Chem. Soc., Faraday Trans. 89* (1993) 2479.
- [6] N. Aihara, K. Torigoe, K. Esumi, *Langmuir* 14 (1998) 4945.
- [7] M. Michaelis, A. Henglein, P. Mulvaney, *J. Phys. Chem.* 98 (1994) 6212.
- [8] M.P. Mallin, C.J. Murphy, *Nano Lett.* 2 (2002) 1235.
- [9] T. Shibata, B.A. Bunker, Z. Zhang, D. Meisel, C.F. Vardeman, J.D. Gezelter II, *J. Am. Chem. Soc.* 124 (2002) 11989.
- [10] I. Srnova-Sloufova, F. Lednický, A. Gemperle, J. Gemperlova, *Langmuir* 16 (2000) 9928.
- [11] S. Link, Z.L. Wang, M.A. El-Sayed, *J. Phys. Chem. B* 103 (1999) 3529.
- [12] Y.W. Cao, R. Jin, C.A. Mirkin, *J. Am. Chem. Soc.* 123 (2001) 7961.
- [13] Y.H. Chen, C.S. Yeh, *Chem. Commun.* (2001) 371.
- [14] I. Lee, S.W. Han, K. Kim, *Chem. Commun.* (2001) 1782.
- [15] N. Sandhyarani, T. Pradeep, *Chem. Mater.* 12 (2000) 1755.
- [16] P. Mulvaney, M. Giersig, A. Henglein, *J. Phys. Chem.* 97 (1993) 7061.
- [17] G. Schmid, *Clusters and Colloids: From Theory to Applications*, VCH, Weinheim, 1994.
- [18] P. Lu, J. Dong, N. Toshima, *Langmuir* 105 (1999) 342.
- [19] R.G. Kreeman, M.B. Hommer, K.C. Grabar, M.A. Jackson, M.J. Natan, *J. Phys. Chem.* 100 (1996) 718.
- [20] L.M. Liz-Marzan, A.P. Philipse, *J. Phys. Chem.* 99 (1995) 15120.
- [21] M.J. Hostetler, C.J. Zhong, B.K.H. Yen, J. Anderegg, S.M. Gross, N.D. Evans, M. Porter, R.W. Murray, *J. Am. Chem. Soc.* 120 (1998) 9396.
- [22] H.Z. Shi, L.D. Zhang, W.P. Cai, *J. Appl. Phys.* 87 (2000) 1572.

- [23] G.C. Papavassiliou, *J. Phys. F: Met. Phys.* 6 (1976) 103.
- [24] R.H. Morriss, L.F. Collins, *J. Chem. Phys.* 41 (1964) 3357.
- [25] R.T. Tom, A.S. Nair, N. Singh, M. Aslam, C.L. Nagendra, R. Philip, K. Vijayamohan, T. Pradeep, *Langmuir* 19 (2003) 3439.
- [26] M. Hansen, K. Anderko, *Constitution of Binary Alloys*, second ed., McGraw-Hill, New York, 1989.
- [27] M. Alejandro-Arellano, T. Ung, A. Blanco, P. Mulvaney, L.M. Liz-Marzan, *Pure Appl. Chem.* 72 (2000) 257.
- [28] M. Sheik-Bahae, A.A. Said, T.H. Wei, D.J. Hagan, E.W. Van Stryland, *IEEE J. Quant. Electron.* 26 (1990) 760.
- [29] M. Anija, J. Thomas, N. Singh, A.S. Nair, R.T. Tom, T. Pradeep, R. Philip, *Chem. Phys. Lett.* 380 (2003) 223.
- [30] G. Mie, *Ann. Phys.* 25 (1908) 377.
- [31] Y. Kim, R.C. Johnson, J. Li, J.T. Hupp, G.C. Schatz, *Chem. Phys. Lett.* 352 (2002) 421.
- [32] M. Moskovits, I. Srnova-Sloufova, B. Vlckova, *J. Chem. Phys.* 116 (2002) 10435.
- [33] H. Yasuda, H. Mori, *Phys. Rev. Lett.* 69 (1992) 3747.
- [34] H. Yasuda, H. Mori, M. Komastu, K. Takeda, *J. Appl. Phys.* 73 (1993) 1100.
- [35] A.S. Nair, T. Pradeep, I. MacLaren, *J. Mater. Chem.* 14 (2004) 857.
- [36] E.F. Lopez, V.S. Escribano, M. Panizza, M. Carnasciali, G. Busca, *J. Mater. Chem.* 11 (2001) 1891.
- [37] A.S. Nair, R.T. Tom, V. Suryanarayanan, T. Pradeep, *J. Mater. Chem.* 13 (2003) 297.
- [38] D.S. Koktysh, X. Liang, B.-G. Yun, I. Pastoriza-Santos, R.L. Matts, M. Giersig, C. Serra-Rodriguez, L.M. Liz-Marzan, N.A. Kotov, *Adv. Funct. Mater.* 12 (2002) 255.
- [39] V. Suryanarayanan, A.S. Nair, R.T. Tom, T. Pradeep, *J. Mater. Chem.* 14 (2004) 2661.
- [40] D. Das, P. Chatterjee, I. Manna, S. Pabi, *Scr. Mater.* 41 (1991) 861.
- [41] A.S. Nair, T. Pradeep, *Curr. Sci.* 84 (2003) 1560.
- [42] F. Hache, D. Ricard, C. Flytzanis, U. Kreibig, *Appl. Phys. A: Solids Surf.* A 47 (1988) 347.
- [43] S.V. Logunov, T.S. Ahmadi, M.A. El-Sayed, J.T. Khoury, R.L. Whetten, *J. Phys. Chem. B* 101 (1997) 3713.
- [44] P.V. Kamat, M. Flumiani, G.V. Hartland, *J. Phys. Chem. B* 102 (1998) 3123.
- [45] L.W. Tutt, T.F. Boggess, *Prog. Quant. Electron.* 17 (1993) 299.
- [46] S.R. Mishra, H.S. Rawat, S.C. Mehendale, K.C. Rustagi, A.K. Sood, R. Bandopadhyay, A. Govindaraj, C.N.R. Rao, *Chem. Phys. Lett.* 317 (2000) 510.
- [47] R.G. Ispasoiu, L. Balogh, O.P. Varnavski, D.A. Tomalia, T. Goodson III, *J. Am. Chem. Soc.* 122 (2000) 11005.
- [48] S. Couris, E. Koudoumas, A.A. Ruth, S. Leach, *J. Phys. Chem. B.* 28 (1995) 4537.
- [49] R. Philip, G. Ravindra Kumar, P. Mathur, S. Ghosh, *Chem. Phys. Lett.* 313 (1999) 719.
- [50] R. Philip, G. Ravindra Kumar, P. Mathur, S. Ghosh, *Opt. Commun.* 178 (2000) 469.